Thermoelectric properties of WSi$_2$–Si$_x$Ge$_{1-x}$ composites

F.W. Dynys [a], A. Sayir [a], J. Mackey [b,*], A. Sehirlioglu [c]

[a] NASA Glenn Research Center, Cleveland, OH 44135, United States
[b] Department of Mechanical Engineering, University of Akron, Akron, OH 44325, United States
[c] Department of Materials Science and Engineering, Case Western Reserve University, Cleveland, OH 44106, United States

ABSTRACT

Thermoelectric properties of the W/Si/Ge alloy system have been investigated with varying concentration levels of germanium and tungsten. The alloys were fabricated by directional solidification with the Bridgman method using boron nitride and fused silica crucibles. The effect of crucible contamination was investigated and found to result in doping the system to suitable levels for thermoelectric applications. The system has been demonstrated as a suitable high temperature p-type thermoelectric material exhibiting high power factors, >3000 µW/m K^2. Seebeck coefficients of the system are on the order of +300 µV/K and electrical conductivities of 2.8 × 10^4 S/m at the optimum operating temperature. The best composition, 0.9 at% W/9.3 at% Ge, achieved a figure of merit comparable to RTG values over the temperature range of interest. The results suggest that W addition can reduce the use of expensive Ge component of the alloy. Reported are the details of processing conditions, microstructure development, and temperature dependent thermoelectric properties. The material system was stable at the temperatures required for NASA's radioisotope thermoelectric generators.

© 2014 Elsevier B.V. All rights reserved.

1. Introduction

Energy consumption is growing at a staggering pace due to global population growth and economic development. Global energy consumption is approaching 50 TW/yr, new power generation strategies are needed to meet the demand. Waste heat is an abundant source that is under-utilized as an energy resource with no additional greenhouse gas emissions. Thermoelectric (TE) technology provides direct conversion of heat to electric power by utilizing the coupled transport of thermal and electrical energy. Space exploration has proven that thermoelectric power generation is highly reliable and exhibits long term operational life [1]. The development of thermoelectric materials with higher conversion efficiencies provides the pathway to expand TE technology into commercial markets such as waste heat recovery. The thermoelectric conversion efficiency of a material is the product of the Carnot efficiency and material conversion efficiency. The conversion efficiency of a thermoelectric material is evaluated by the dimensionless figure of merit (ZT):

$$ZT = \frac{\sigma \alpha^2}{\lambda} T \tag{1}$$

where α is the Seebeck coefficient, σ is the electrical conductivity, λ is the total thermal conductivity, and T is the absolute temperature. Total thermal conductivity λ includes heat conduction by both the lattice and charge carriers. The inter-dependency of the material properties (α, σ, λ) has plagued the development of high efficiency TE materials. Historically, ZT improvements have been achieved by alloying, which causes strong phonon scattering. Reduction in thermal conductivity achieved by alloying is usually offset by deterioration in electrical transport, limiting ZT enhancement.

Technology advancement has led to higher ZT by decoupling TE property inter-dependency via microstructural engineering, which provides a method to control phonon transport by scattering dominant phonon wavelengths without detrimental effect on electrical transport. For high temperature applications, the majority of phonons are most effectively scattered by inclusions at the nano-scale as a result of greater interface area per unit volume of the inclusions as well as enhanced distribution of the inclusions in the matrix. Semi-metallic nano-particles enhance electrical properties as demonstrated by ErSb particles in a GaSb matrix and ErAs particles in InGaAlAs [2]. Similarly for the Si$_x$Ge$_{1-x}$ system nano-particle in Si$_x$Ge$_{1-x}$ have been investigated both theoretically [3,4] and experimentally for the Si$_{80}$Ge$_{20}$–CrSi$_2$ [5] and Si$_{80}$Ge$_{20}$B$_{06}$–Er [6] systems.

Directional solidification of off-eutectic and eutectic-compositions is well-known to yield self-assembled microstructures that are non-achievable by solid state sintering. The self-assembled

structure can be controlled or engineered by process variables and material volume fraction. Additionally, formation of low energy coherent interfaces and textured/oriented microstructures often occur by directional solidification. Unfortunately directional solidification is not well suited to obtain the desirable nano-structured materials, as grain growth is promoted by the long solidification time. Solidification techniques have been reported for TE systems of $Bi_{0.5}Sb_{1.5}Te_3$ [7], $PbTe–Sb_2Te_3$ [8], PbTe–Si [9], $Pb_{1-x}Sn_xTe–PbS$ [10], $AgPb_mSbTe_{2-m}$ [11], Ag–Pb–Te [12], and Si–Ge [13–19].

Due to their abundance, low cost and low toxicity, metal silicides have been investigated as potential high temperature TE materials [20]. A recent work that has focused on Mg–Si alloys achieved ZT > 1 [21]. Additional interest has arisen for Si–Ge composites from modeling work. Computations indicate that a strong reduction in thermal conductivity can be achieved in Si–Ge alloys containing metal silicide nanoparticles [3]. We have investigated directional solidification of a number of M–Si and M–Ge–Si (where M = Ti, Mo, W, Cr, Zr, Ta, V) systems [22]. Directional solidification in these systems does not yield an alloy containing nanoparticles. However, the Si–Ge–W system exhibits good TE properties.

Investigation centered on minor addition of W ($\leqslant$3 at%) to Si_x-Ge_{1-x} alloys. The W addition forms metallic WSi_2 inclusions with a melting point of 2437 K. Metallic inclusions in thermoelectric materials are an untraditional approach for TE composites. The work shows that the addition of WSi_2 can reduce Ge content by 50% for optimal thermoelectric performance.

2. Experimental procedure

Directional solidification was accomplished using the vertical Bridgman method. Starting materials for ingot preparation were ~5 mm silicon granules (Cerac, Milwaukee, WI, $\geqslant$99.9%), 100 mesh germanium powder (Alfa Aesar, Ward Hill, MA, $\geqslant$99.9%) and 100 mesh tungsten powder (Alfa Aesar, $\geqslant$99.9%). Alloys were melted in a helium atmosphere in a graphite resistance heated furnace (Thermal Technology LLC, Santa Rosa, CA). Temperature was controlled by an optical pyrometer. Boron nitride (BN) (Momentive Performance Materials, Albany, NY) and fused silica (SiO_2) (Momentive Performance Materials, Albany, NY) crucibles were used. Calcium chloride ($CaCl_2$) was added to the SiO_2 crucible as an interfacial material between crucible and melt; eliminating mechanical failure of the crucible during sample cooling [23]. Ingots were prepared through two solidification runs. The first solidification served to consolidate the raw material into an ingot. Processing temperatures ranged from 1798 K to 1973 K with soak times of 1–3 h. After the first solidification, additional raw material was added to achieve a 30–40 g sample with approximate dimensions of 20 mm in length and 22 mm in diameter. The second solidification included directional solidification with a pull rate of 200 mm/h over the temperature gradient that naturally exists in the furnace. The measured temperature gradient was 8.5 K/mm. The high pull rate is greater than the pull rates recommended (<10 mm/h) to avoid constitutional undercooling [24]. It should be noted that zone leveling was not performed on the specimens presented in this work; rather the specimens were investigated as obtained at the completion of the second solidification run.

Measurement of the Seebeck coefficient and electrical conductivity were made simultaneously using a ZEM-3 Seebeck Coefficient/Electrical Resistance Measurement System (Ulvac Technologies, Methuen, MA). The system performs a four-point electrical conductivity measurement while simultaneously measuring the Seebeck coefficient and temperature differential using two type-K thermocouples. Seebeck coefficient of the type-K thermocouples was automatically compensated by the software. A temperature gradient was established across the specimen by a platinum heater mounted in the lower support arm. Specimen dimensions were $4 \times 4 \times 18$ mm. Measurement was performed in a helium atmosphere at 85 Torr, a temperature range of 373–1273 K and thermal gradients ranging from 0.4 to 0.7 K/mm were employed. A temperature stability of ±0.25 K was maintained over the course of the measurement at each temperature step.

The thermal conductivity (λ) of specimens was calculated from thermal diffusivity (D), heat capacity (C_p) and density (ρ): by the relation $\lambda = \rho D C_p$. Thermal data was measured in the temperature range of 373–1273 K by the laser flash method (Anter Flashline 5000, Anter Corporation, Pittsburgh, PA); density was determined by sample mass and geometric dimensions. Measurements followed ASTM E1461. Pyroceram was used as the standard for each measurement to calculate specific heat of samples, detector was liquid nitrogen cooled InSb. Samples were cut from the ingots with thickness of 2–3 mm and diameter of 12.5 mm. Samples were platinum coated with <1 μm thickness by physical vapor deposition (Lesker PVD-75, Kurt J. Lesker Corporation, Jefferson Hills, PA); ensuring an opaque surface to laser irradiation. Platinum thickness is negligible when compared to the specimen thickness, therefore is not believed to alter thermal measurements significantly. Specimens were also coated with carbon paint in accordance with standard flash method to ensure a consistent repeatable emissivity. Three measurements were taken for each sample per temperature and the results were averaged. The time–temperature curves were analyzed by the method of Clark and Taylor [25].

Due to ingot physical constraints, samples obtained for thermal conductivity and electrical measurement could not be obtained with the same orientation. Thermal conductivity samples coincide with the axial direction of the ingot, while electrical samples were obtained in the radial direction (perpendicular to pull direction). Microstructural investigation indicated isotropic structures in both axial and radial directions, diminishing the effect of orientation.

Microstructural characterization was performed with a Hitachi S-4700 field emission scanning electron microscope (Hitachi High Technologies, Gaithersburg, MD) equipped with energy dispersive X-ray spectroscopy (EDS) (EDAX, Mahwah, NJ). Other characterization included inductively coupled plasma mass spectroscopy (ICP) with a Varian Vista Pro (Varian, Palo Alto, CA), X-ray diffraction (XRD) on a D-8 Advance (Bruker, Billerica, MA), and oxygen nitrogen determination with a TC-436 (Leco, St. Joseph, MI).

3. Results and discussion

3.1. Microstructure

All specimens showed similar microstructures, an example of which is shown in the back-scattered SEM micrograph in Fig. 1 (taken at 15 kV) for an alloy containing 0.9 at% W and 9.3 at% Ge (sample 3 in Table 1). Chemical mapping by EDS is also added to show the Si, Ge and W distribution in the microstructure. Large 10–100 μm faceted precipitates were observed in the matrix. Chemical map shows that the entire W content is contained within the precipitates. Precipitates were identified as WSi_2 via XRD (Fig. 2). Determination of crystal growth habits was not integral to this investigation. Solidified microstructures are irregular with very little indication for preferred ordering of the WSi_2 phase. The solidification parameters inevitably lead to a considerable amount of Ge segregation resulting in a non-uniform matrix as shown in Fig. 1. Although Si and Ge exhibit complete solid state solubility, it is well known that solidification is non-congruent with the melt [13]. Local Ge concentration content was determined through standard less EDAX ZAF quantification. For sample 3, with a nominal 9.3 at% Ge content, the Ge segregation ranged from 6.4 to 15.6 at% Ge. Although Ge segregation is intrinsic from the solidification process, the Ge rich areas of the samples tend to coincide near or surrounding the WSi_2 precipitates. In the micrograph shown (Fig. 1) the areas with the highest Ge concentration are either adjacent to, or enclosed by the WSi_2 precipitates. This is likely due to a Ge rich boundary layer that forms as Ge was rejected from the WSi_2 precipitates during crystallization. Thus, this silicide precipitation aids in Ge driven micro-segregation which may help explain some of the composite properties introduced later in Section 3.3. Thermoelectric properties. Fig. 2 shows powder XRD pattern for $Si_{89.8}Ge_{9.3}W_{0.9}$. XRD of a melt derived $Si_{90}Ge_{10}$ is included for comparison. Both samples have the same Si/Ge ratio and were solidified under identical conditions. Additional peaks present in the W containing sample correspond to tetragonal WSi_2 precipitates. The XRD patterns shown in Fig. 2 are typical for all the W/Si/Ge compositions investigated.

Rietveld refinement was performed using Topas (Bruker) software. The WSi_2 phase was analyzed over a 2Θ range of 30–45° to exclude reflections from the Si_xGe_{1-x} phase. Data was acquired in a Bragg–Brentano configuration with 300 mm radius, 4° sollers, at a rate of 3.5° per min. The model had a Rexp value of 4.51 and GOF value of 1.27, lattice parameters and Lorentzian crystallite domain size were the parameters of study in the model. The data analysis shows crystallite domain size of 238 nm with tetragonal lattice parameters of $a = b = 0.321$ nm and $c = 0.783$ nm. The measured lattice parameters match the reported values for WSi_2, $a = b = 0.32138$ nm and $c = 0.78299$ nm [26]. XRD results indicate that the large WSi_2 precipitates are polycrystalline. The Si_xGe_{1-x}
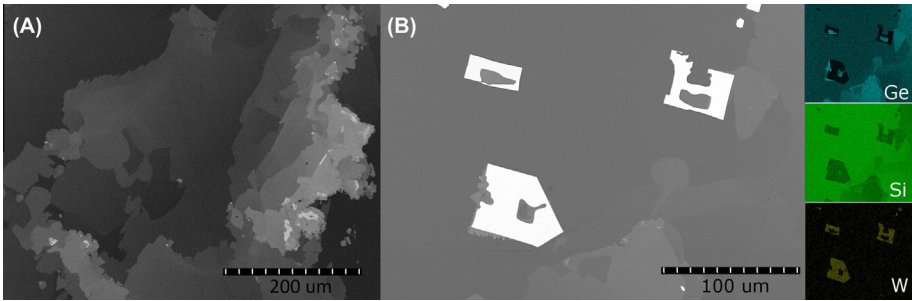
Fig. 1. Back-scattered SEM images (A and B) with EDS chemical maps (right) of Ge, Si, and W. Large WSi_2 precipitates (white faceted precipitates) can be observed in an inhomogeneous Si/Ge matrix.

Table 1
Nominal compositions of the specimens studied.

#	Si (at%)	Ge (at%)	W (at%)	Si (wt%)	Ge (wt%)	W (wt%)
1	99.2	0.0	0.8	95	0	5
2	94.8	4.3	0.9	85	10	5
3	89.8	9.3	0.9	75	20	5
4	84.3	14.9	0.8	66	30	4
5	82.4	14.6	3.0	59	27	14
6	77.6	19.4	3.0	53	34	13
7	72.7	24.3	3.0	47	40	13

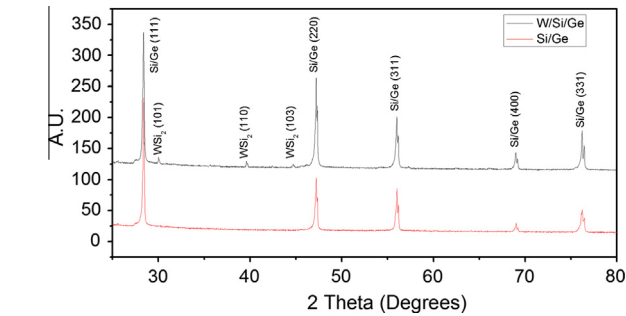**Fig. 2.** XRD Pattern for sample 3, $Si_{89.8}Ge_{9.3}W_{0.9}$ (top), and $Si_{90}Ge_{10}$ (bottom), addition of W forms WSi_2 second phase with no shift in Si/Ge reflections [26,27].

matrix could not be accurately represented by the model, making quantitative phase analysis impractical [27]. Model failure arises from compositional peak broadening due to Ge segregation. The compositional fluctuations cause fluctuations in lattice constant which creates strain and dislocations. Thus, crystallite size and lattice strain could not be de-convoluted from the XRD data for the Si/Ge matrix. A more advanced fitting technique must be employed in order to account for the peak broadening due to the range of alloying present, such a model has been presented in the work of Leineweber and Mittemeijer [28]. The average matrix lattice parameter from the Si_xGe_{1-x} peak positions revealed predominate cubic lattice parameter of 0.544 nm for both compositions. This Si_xGe_{1-x} lattice parameter is in good agreement with the work of Dismukes et al. [14], reporting a lattice parameter for $Si_{90}Ge_{10}$ composition as 0.545 nm. The introduction of W into the system had no observable effect on the lattice spacing of the bulk matrix, suggesting that little to no W is soluble into the Si_xGe_{1-x} matrix.

Jackson and Hunt [29] developed a method to predict eutectic microstructures based upon entropy of fusion. Theory states that phases with high entropy of formation (ΔS_f) form faceted interfaces when $\Delta S_f/R > 2$ (where R = gas constant). The entropies of formation of interest in this system are roughly $\Delta S_{Si} \sim 30$ J/K mol, $\Delta S_{Ge} \sim 30$ J/K mol [30], and $\Delta S_{WSi2} \sim 18$ J/K mol [31]. The dimensionless $\Delta S_f/R$ values are >2, Si and Ge exhibiting $\Delta S_f/R$ of 3.6 and

2.1 for WSi_2, crystal growth favors faceted precipitates. Growth direction of the faceted phase is determined by the specific crystallographic orientations. Thus, directional growth is not necessarily controlled by the thermal gradient of solidification. We have observed a large number of Si systems that exhibit faceted growth: $Si-MoSi_2$, $Si-Ge-MoSi_2$, $Si-ZrSi_2$, $Si-VSi_2$ and $Si-TaSi_2$. Contradictory to Jackson and Hunt model, rod growth has been reported for $Si-TiSi_2$ [22] and $Si-CrSi_2$ [32].

3.2. Crucible selection

The crucible selection was found to be a critical process parameter. All specimens were solidified under identical parameters using BN and SiO_2 crucibles. In order to prevent reaction between SiO_2 crucible and Si/Ge/W melts, 1.5 g of $CaCl_2$ powder was added to the charge. Liquid $CaCl_2$ forms a barrier between the melt and SiO_2 crucible, which eliminated fracturing of the ingot during cooling. Residual $CaCl_2$ on the ingot surface was removed by rinsing with water [23].

Fig. 3 shows the temperature dependent resistivity data for sample 3 ($Si_{89.8}Ge_{9.3}W_{0.9}$) solidified in BN and SiO_2 crucibles. The $Si_{89.8}Ge_{9.3}W_{0.9}$ alloy processed in SiO_2 crucible exhibits a high electrical resistivity and extrinsic to intrinsic semiconductor behavior around 773 K. In conjunction with extrinsic to intrinsic electrical transport behavior, the alloy transitioned from p-type to n-type Seebeck behavior. However, the same alloy processed in BN crucible exhibited a lower electrical resistivity and p-type extrinsic semiconductor behavior over the measured temperature range. Thus, electrical behavior is consistent with B doping.

Chemical analysis of the specimens was performed to provide B and N concentrations. Fig. 4 shows that sample 3 ($Si_{89.8}Ge_{9.3}W_{0.9}$) processed in a BN crucible had significantly higher B content (0.17 at%) than the specimen derived from the SiO_2 crucible (0.009 at%). The N content was low ($\leqslant$0.04 at%) but it was twice as high for the sample derived from BN crucible. The B concentration
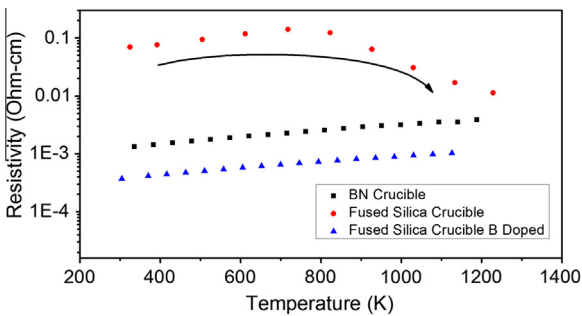

Fig. 3. Electrical resistivity of three comparable samples prepared using BN or SiO_2 crucibles. Trend indicates un-intentional doping resulting from the BN crucible.
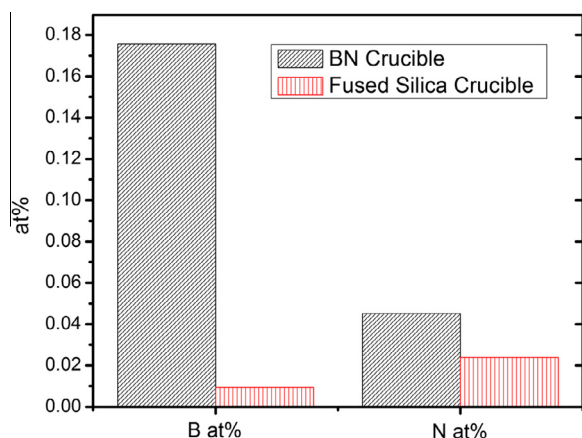
Fig. 4. Compostion for ingots prepared in BN and SiO$_2$ crucibles as determined by ICP and Nitrogen determination. Samples are not intentionally doped.
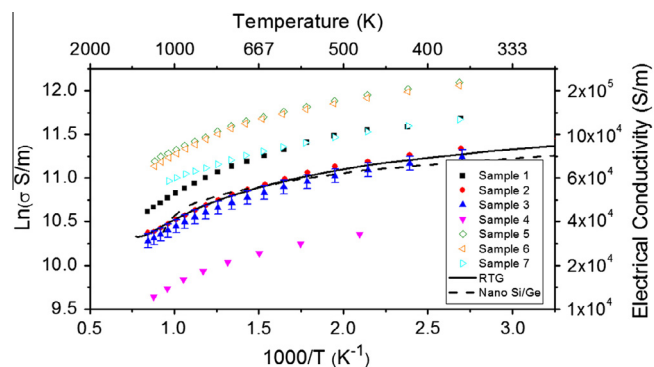

Fig. 5. Arrhenius plot of electrical conductivity of several W/Si/Ge samples. Closed symbols represent 0.8 at% W, open symbols 3 at% W. Included are published values for RTG [13] and nano-structured [15] Si$_{80}$Ge$_{20}$ alloys.

from the sample derived from the fused silica crucible was unexpected. The most probable cause was the CaCl$_2$, purity level was 99%. Chemical analysis of the W raw powder showed 0.0003 at% B impurity. The B level in the Si and Ge starting materials was below the instrument detection limit. B was not observed in the microstructure as either B precipitate or within the matrix, especially near the BN-melt interface. XRD also displayed no evidence of second phases formed due to B contamination or lattice parameter shift. Optimizing the B content can be beneficial in optimizing the TE properties in the W/Si/Ge system. To emphasize this point a third specimen was prepared by intentional doping of Si$_{89.8}$Ge$_{9.3}$W$_{0.9}$ with 1.9 at% B and processed in SiO$_2$ crucible; the electrical resistivity is also shown as a function of temperature in Fig. 3. The temperature dependent electrical resistivity behavior is similar to the ingot processed in BN crucible, exhibiting extrinsic semiconductor behavior for the whole temperature range. The absolute values of the electrical resistivity were lower due to the larger B-doping.

The rest of this paper focuses on specimens processed in BN crucibles. For consistency, all BN crucibles were filled to the same levels and subjected to similar solidification profiles. This ensured the contact area, and dopant diffusion kinetics were comparable between samples. Additionally, the thermodynamic solubility limit of B in Si serves to provide a consistent upper limit. Typical RTG samples are doped to the solubility limit, as dopant segregation is a commonly reported phenomenon [33,34]. Since the electrical properties of these samples are similar to RTG properties, the doping levels provided by the crucibles are also likely to be near the solubility limit. As a result the sample set is believed to have comparable doping levels, although a controlled doping scheme using SiO$_2$ crucibles may be preferable for future work.

3.3. Thermoelectric properties

Fig. 5 shows an Arrhenius plot of electrical conductivity as a function of temperature and composition for all samples processed in BN crucibles. Reported results for p-type Si$_{80}$Ge$_{20}$ are also included in Fig. 5 for melt derived RTG (zone leveled) [13] and sintered nano-structured materials [15]. The temperature dependent behavior of electrical conductivity was very similar to published results for p-type B doped Si$_{80}$Ge$_{20}$. With increasing temperature the electrical conductivity decreased over the temperature range of 373–1273 K. Composition did not have any effect on the temperature dependent behavior. All the samples exhibited the characteristics of a degenerate semiconductor, metal like σ–T relationship. None of the samples exhibit intrinsic conduction behavior up to 1273 K, the instrumentation limit. For clarity, data uncertainty

was calculated for sample 3 and represents typical measurement uncertainty for all samples. Uncertainty calculations include geometric tolerance of samples/measurement configuration, statistical variation, and multimeter uncertatinty. The details of the uncertatinty analysis will be published in the near future. Typical uncertainties are on average ±7.9%. The observed trend in electrical conductivity for the investigated compositions is a uniform reduction in conductivity with increasing Ge concentration (Specimens 1–4 shown with solid symbols, Fig. 5) at a given W concentration (0.8 at%). This trend can be understood from the disorder introduced in the matrix as Ge occupies Si lattice sites. Ge on Si sites introduce fluctuations in lattice potential, strain and crystalline defects that result in an extra electron scattering term, which is proportional to the fraction of Ge in the alloy [18]. Alloy scattering is non-existent for sample 1 containing no Ge, exhibiting a higher electrical conductivity than Ge containing samples. Samples 2–4 have increasing levels of Ge content where alloy scattering caused a uniform reduction in electrical conductivity. On average electrical conductivity decreased 68.2% with an increase of Ge content from 0 to 14.9 at% Ge. The samples containing 4.4 and 9.3 at% Ge (samples 2 and 3) exhibit similar electrical conductivity to the published data for both zone-refined and nano-structured p-type Si$_{80}$Ge$_{20}$ [13,15].

Increasing the W content increased the electrical conductivity (samples 4 and 5) at similar Ge concentrations. Increasing the W at% content from 0.8% to 3% (shown with open symbols, Fig. 5) resulted in an enhancement of 79% in the electrical conductivity on average. Er additions to Si have been reported by Zhao et al. to enhanced electrical conductivity [6]. The work of Nonomura et al. has reported WSi$_2$ to be a narrow gap p-type semiconductor with an activation energy of 0.005 eV and electrical conductivity of 2.5E4 S/m near room temperature [35]. The reported electrical conductivity of WSi$_2$ is lower than all the samples measured in this work. Therefore, the increase in electrical conductivity observed between samples 4 and 5 cannot be explained directly by the presence of the WSi$_2$ phase. The trend is instead believed to be due to the change in carrier density as a result of the two W levels. Samples 1–3 with 0.8 at% W have carrier densities ranging from 1.2E20 cm^{-3} to 2.9E20 cm^{-3} while sample 5 with 3 at% W has 8.5E20 cm^{-3}. As discussed in a previous Section 3.1 the W is only observed in the precipitates and is not detected in the matrix. Therefore, the carrier density difference may be a result of the silicide phase influencing the solubility limit and kinetics of B in the Si$_x$Ge$_{1-x}$ matrix. Further work is needed to elucidate the enhanced transport mechanism.

The effect of Ge content on the electrical conductivity shows some dependence on W content. In both W cases, there is an optimal Ge concentration and higher Ge concentrations lead to

reduction in electrical conductivity. The higher W concentration allows higher Ge addition. Thus, the data shows that a combination of WSi_2 and Ge additions can control electrical conductivity. Reduction in Ge content helps in reducing material cost.

The temperature dependence of Seebeck coefficient for the same set of samples is shown in Fig. 6. All samples exhibited p-type behavior over the temperature range investigated. The measured values fell in the range of 70–300 µV/K. Seebeck coefficient increased with temperature; typical behavior for a degenerate extrinsic semiconductor. For clarity, uncertainty in the data is reported for sample 3 and represents typical uncertainties of all samples. The uncertainty accounts for the probe wire Seebeck uncertainty, statistical variation, multimeter uncertainty, and the cold finger effect. The cold finger effect is an artifact of the four point measurement configuration, in which heat is parasitically transferred down the probe length. The effect leads to an over-estimation of the Seebeck coefficient. The total uncertainty was estimated with a thermal FEA along with standard measurement error propagation. The uncertainty ranges from ±2% near room temperature to ±2%–17% at high temperature. The asymmetry of the uncertainty at high temperature is due to the cold finger effect. The 0.8 at% W samples (shown with solid symbols, Fig. 6) all exhibit Seebeck coefficients higher then published values for p-type $Si_{80}Ge_{20}$ [13,15]. At low temperature the Seebeck coefficients decrease slightly with increasing Ge content (samples 1–4). The high Seebeck coefficient combined with comparable electrical conductivity leads to power factor improvements as large as 50% over RTG. Seebeck enhancement of PbTe has been discussed by Faleev and Leonard [36] by introducing metallic precipitates into a PbTe matrix. Band bending at the interface can filter low energy electrons and leave high energy electrons undisturbed, leading to enhanced Seebeck coefficient and power factor for the composite. This observed trend due to electron filtering phenomenon was dependent on precipitate size and can therefore not explain the trend observed in this micron-scale system reported here. Further work is required to understand the dependence of carrier concentration and mobility with temperature. At this time the enhancement of power factor is not clearly understood. The 3 at% W samples (shown with open symbols, Fig. 6) have lower Seebeck coefficients then the 0.8 at% samples. The decrease is consistent with carrier concentration data, which is higher for the 3 at% W samples.

Fig. 7 shows the total thermal conductivity of the compositions investigated and the lattice thermal contribution calculated by the Wiedemann–Franz law. Uncertainty on total thermal conductivity is estimated to be ±5% [37]. The uncertainty in lattice thermal conductivity is calculated based on both the electrical conductivity and the thermal conductivity. The data shows that WSi_2 is not effective in reducing thermal conductivity; sample 1 exhibits thermal conductivity 57.7–15.5 W/m K in the temperature range of

295–1173 K (Fig. 7A). The addition of Ge is effective in reducing the thermal conductivity significantly over the entire temperature range of interest; the inset shows that Ge; reduced the thermal conductivity to <12 W/m K. After the initial large reduction in thermal conductivity, smaller reductions were obtained with increasing Ge concentration, samples 2–4. However, there was no observable trend in thermal conductivity with higher Ge concentrations.

A least squares regression was used to interpolate thermal conductivity data in order to calculate the lattice thermal contribution and ZT. The correlation coefficient of the thermal data ranges from 0.76 to 0.98, the statistical uncertainty of the measurement data is understood to provide low correlation, but the regression is still thought to provide accurate averages for the purpose of calculating figure of merit and lattice contribution. A more complicated fitting method would model the statistical variation of the measurement rather than focusing on capturing the representative values. The Wiedemann–Franz law estimates the lattice contribution of thermal conductivity as follows:

$$\lambda_{Lat} = \lambda_{Total} - L\sigma T \tag{2}$$

$$L = \frac{\pi^2 k_b^2}{3e^2} \tag{3}$$

where λ_{Lat} is the lattice thermal contribution, λ_{Total} the total thermal conductivity, T the temperature, σ the electrical conductivity, and L Lorenz number. The Lorenz number is classically approximated from k_b the Boltzmann constant and the charge of an electron e, $L = 2.44E{-}8\ W\,\Omega\,K^{-2}$.

Lattice thermal conductivity decreased significantly with the initial increase in Ge content. As the Ge content increased further samples 2 to 4, smaller reductions in the lattice thermal conductivity was observed, with values almost unchanged between specimens 3 and 4 for the whole temperature range. The trend is understood as a result of phonon scattering by the mass difference of Si and Ge [14,16,17,19]. Increasing the W content, sample 4 to 5, resulted in a minor decrease in lattice thermal conductivity; as the total thermal conductivity remained similar despite increasing electrical conductivity. The alloy composition with the lowest lattice thermal conductivity was specimen 5 with values similar to the lattice thermal conductivity of published data for p-type RTG $Si_{80}Ge_{20}$ [13]. The higher lattice thermal conductivities of the samples, as compared to RTG, were due to a combination of the lower Ge content and the observed micro-segregation in the samples (Fig. 1). The work of Lee and Hwang [38] theoretically demonstrated the importance of homogeneous segregation of the Si/Ge matrix. In the simulations of Lee and Hwang, clusters of Ge atoms were found to significantly increase the thermal conductivity, as clusters of Ge atoms reduced the number of Si–Ge bonds which provided the desired phonon scattering. Increases as large as 3x were calculated for Ge precipitates of 2 nm [38]. The trend in samples 5–7 was counter intuitive as conductivity increases with increasing Ge content. The behavior may be a result of increased micro-segregation of the Ge as a result of the higher 3 at% W phase. In the previous Section 3.1 Ge segregation was observed to be correlated with the silicide precipitates. The higher W content may be driving more Ge micro-segregation, leading to increased conductivity.

The 10–100 µm scale of precipitates and low volume fraction of the composites allows for a straight-forward estimation of the thermal conductivity. The precipitate/matrix interface surface area, normalized with bulk volume, was estimated to be 10 cm^2/cm^3 for the samples in this study. To provide a contrast, the surface area per volume of a nano-structured composite containing 10 nm precipitates has on the order of 1E5 cm^2/cm^3. The surface area is calculated employing the range of volume fractions for the samples in this work. The influence of phonon scattering at the interface of
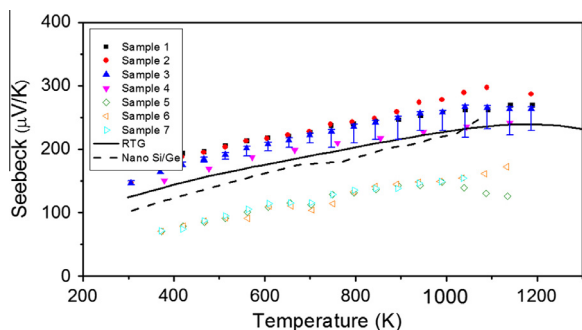

Fig. 6. Seebeck coefficient of several W/Si/Ge samples. Closed symbols represent 0.8 at% W, open symbols 3 at% W. Included are published values for RTG [13] and nano-structured [15] $Si_{80}Ge_{20}$ alloys.
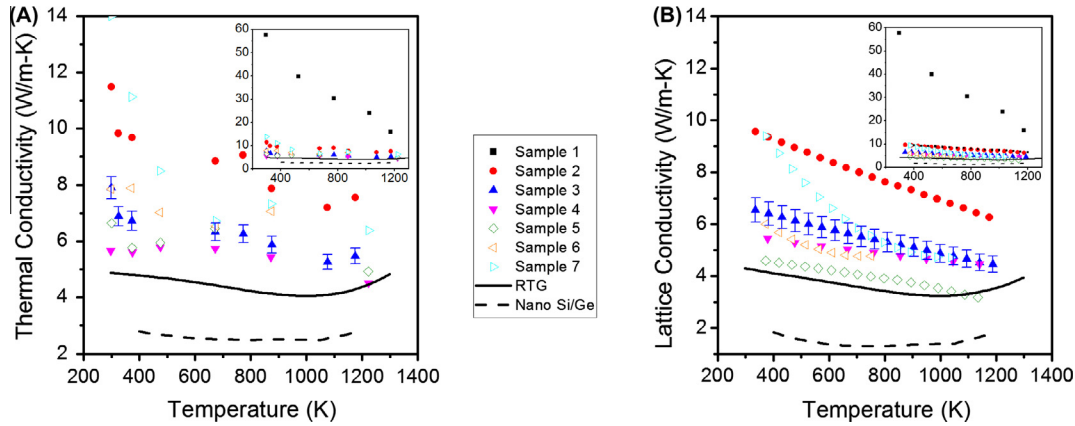
Fig. 7. (A) Total thermal conductivity of several W/Si/Ge samples. (B) Calculated lattice thermal conductivity component. Closed symbols represent 0.8 at% W, open symbols 3 at% W. Included are published values for RTG [13] and nano-structured [15] $Si_{80}Ge_{20}$ alloys.

the silicide precipitates should be negligible for the samples of this work. Therefore a straight-forward estimation of thermal conductivity can be based on considering the samples as composite bodies of two phases, the Si_xGe_{1-x} matrix and WSi_2 precipitates. As previously discussed, the thermal conductivity of the matrix will be strongly dependant on the alloying level of Si_xGe_{1-x} [14,16,17,19]. Additionally, the dopant level will have a large influence on thermal conductivity as point scattering inhibits phonon transport. To gain a deeper understanding, without unneeded complexity, the matrix of the samples is assumed to be homogeneous, i.e. no micro-segregation of Si_xGe_{1-x}, with doping levels comparable between samples. The precipitates are modeled as a periodic arrangement of tungsten silicide cubes with side length (d) of 50 μm. Fig. 8 shows the simplified model of the composite, with the repeating unit highlighted. The geometry of the repeating unit (captured by x and the precipitate size d) is a function of the area fraction (γ) of the precipitate phase, which can be estimated from the nominal volume fraction of the silicide phase.

$$x = \frac{d(\sqrt{4+\gamma} - 3\sqrt{\gamma})}{2\sqrt{\gamma}}$$ (4)

$$\lambda_{Composite} = \frac{(2d+x)}{(d+x)}\left[\frac{x \cdot \lambda_{Matrix}}{(2d+x)} + \frac{1}{\frac{(d+x)}{d \cdot \lambda_{Matrix}} + \frac{1}{\lambda_{Precipitate}}}\right]$$ (5)

The composite thermal conductivity can be estimated by considering the series/parallel nature of the components of the repeating unit. The method employed is classically used for the analysis of composite bodies under steady thermal conduction [40]. Table 2 shows the predicted influence of the silicide phase on the samples. The silicon at% used for the calculations are the nominal level of silicon minus the silicon consumed by the silicide phase. These levels compare well to average values measured with EDS. The matrix thermal conductivity is calculated based on the experimental work of Maycock [16]. The silicide volume fraction is used to establish the geometry of the model. For sample 1 the matrix is 100% Si and the nominal silicide volume fraction is 1.7%, Table 2. As a result of the volume fraction the model x parameter is calculated to be 307 μm. The calculated composite conductivity 59.3 W/m K is lower than the matrix conductivity 59.6 W/m K, as a result of the relatively lower conductivity of the precipitate phase 46.6 W/m K. The calculated conductivity for sample 1 matches reasonable well with the measured value 60 W/m K. For the remaining samples 2–7 the calculated composite conductivity are higher than the matrix conductivity as a result of the precipitates. The precipitate driven increase in thermal conductivity is undesirable for these samples, but the calculation shows an average increase of 1.6% for the 0.8 at% W samples and 7.1% for the 3 at% W samples. Compared to the 50% improvement of electrical properties the WSi_2 precipitates are found to be desirable. For samples 1–4 the calculated
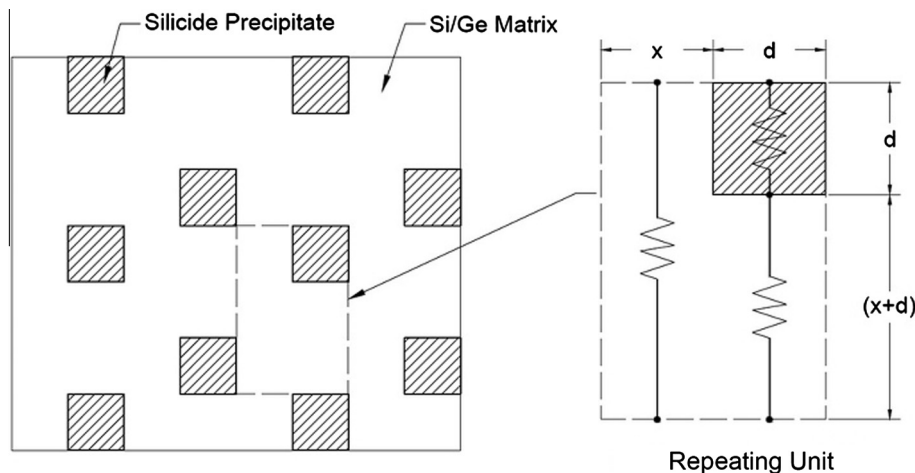

Fig. 8. Schematic diagram of Si/Ge matrix with silicide precipitate. Repeating unit highlighted to the right to outline the geometric parameters x and d.

Table 2
Calculated thermal conductivity of composite samples.

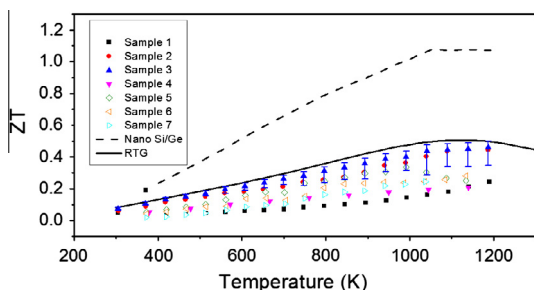| Sample #	Si at% in matrix	Silicide V.F.%	Thermal conductivity (W/m K) at 300 K			
			Matrix [26]	Precipitate [39]	Composite calculated	Measured
1	100.0	1.7	59.6	46.6	59.3	60
2	95.6	1.8	14	46.6	14.2	12
3	90.5	1.9	8.8	46.6	8.96	8
4	84.8	1.7	6.8	46.6	6.91	6
5	84.0	6.5	6.8	46.6	7.26	7
6	78.7	6.4	4.8	46.6	5.15	8
7	73.4	6.4	4.4	46.6	4.72	14

Fig. 9. Figure of merit (ZT) of several W/Si/Ge samples. Closed symbols represent 0.8 at% W, open symbols 3 at% W. Included are published values for RTG [13] and nano-structured [15] $Si_{80}Ge_{20}$ alloys.

composite conductivities compare well with the measured data, while samples 5–7, with 3 at% W, show poor comparison between the model and the actual data. The deviation could be explained by the Ge micro-segregation driven by the WSi_2 phase, discussed in Section 3.1. Ge micro-segregation is well known to drastically alter thermal conductivity [38] and is unaccounted for in the matrix conductivity of the model.

The figure of merit is shown in Fig. 9. Similar to $Si_{80}Ge_{20}$ alloy, the ZT increases in value over the measured temperature range. Trends in Seebeck coefficient as a function of composition dominated the trends in the calculated ZT values for a given W content. ZT maximized for the specimen 3 for the whole temperature range. At higher Ge contents (samples 5–7) the ZT did not change in any significant amount similar to the observations in Seebeck coefficient. However, electrical conductivity was the dominant factor in deciding the trends in ZT as a function of W content; thus the ZT increased slightly with increasing W content, samples 4–5, despite a decrease in Seebeck coefficient. This was due to the greater increase in electrical conductivity even though the ZT changes with square of Seebeck coefficient. The optimal composition from this investigation with a ZT near RTG was found to be 0.8 at% W/ 9.3 at% Ge (sample 3). This sample was created without the need for lengthy, thus costly, zone leveling. The results suggest that W addition can reduce the use of expensive Ge component of the alloy.

4. Conclusion

The work presented has demonstrated the feasibility of a W/Si/ Ge system for high temperature thermoelectric applications. Directional solidification in the W/Si/Ge system resulted in formation of randomly ordered WSi_2 precipitates in the micron-size range, exhibiting faceted growth. The large separation of the solidus and liquidus lines during solidification leads micro-segregation of Ge. Processing in BN crucibles resulted in B dissolution in the melt on the order of 0.17 at%. The results show that a combination of WSi_2 and B can affect electrical transport, reduction in Ge concentration can lead to potential cost savings. The ability to control the

dopant level through the use of more readily available fused silica crucibles provides a potential pathway for optimizing the system.

W addition with B doping enhances electrical properties. Seebeck coefficients on the order of +300 μV/K along with electrical conductivities around 2.8×10^4 S/m and high power factors up to 3,000 μW/m K^2 in the temperature range of 373–1173 K was observed. The highest power factor was achieved at a composition of $Si_{89.8}Ge_{9.3}W_{0.9}$; a 50% higher power factor is observed than published results for sintered and zone-leveled $Si_{80}Ge_{20}$. Strong electrical properties combined with good thermal conductivity resulted in a figure of merit comparable to the traditional high temperature Si_xGe_{1-x} materials developed by NASA for use in RTGs (ZT = 0.5).

References

[1] W.P. Lange, R.G. Carroll, Review of recent advances of radioisotope power systems, Energy Convers. Manage. 49 (2008) 393.
[2] J.M.O. Zide et al., High efficiency semimetal/semiconductor nanocomposite thermoelectric materials, J. Appl. Phys. 108 (2010) 123702.
[3] N. Mingo et al., Nanoparticle-in-alloy approach to efficient thermoelectrics: silicides in SiGe, Nano Lett. 9 (2009) 711.
[4] Y. Ezzahri, K. Joulain, Effect of embedding nanoparticles on the lattice thermal conductivity of bulk semiconductor crystals, J. Appl. Phys. 113 (2013) 043510.
[5] Z. Zamanipour, D. Vashaee, Comparison of properties of p-type nanostructured bulk $Si_{0.8}Ge_{0.2}$ alloy with $Si_{0.8}Ge_{0.2}$ composites embedded with $CrSi_2$ nano-inclusions, J. Appl. Phys. 112 (2012) 093714.
[6] R. Zhao, L. Shen, F. Guo, Enhanced electrical conductivity in $Si_{80}Ge_{20}B_{0.6}$ alloys with Er addition prepared by spark plasma sintering, J. Mater. Res. 26 (2011) 1879–1885.
[7] A.M. Dehkordi, D. Vashaee, Enhancement in thermoelectric power factor of polycrystalline Bi0.5Sb1.5Te3 by crystallite alignment, Phys. Status Solidi (A) 209 (2012) 2131.
[8] T. Ikeda et al., Self-assembled nanometer lamellae of thermoelectric PbTe and Sb_2Te_3 with epitaxy-like interfaces, Chem. Mater. 19 (2007) 763.
[9] J.R. Sootsman et al., Microstructure and thermoelectric properties of mechanically robust PbTe–Si eutectic composites, Chem. Mater. 22 (2010) 869.
[10] J. Androulakis et al., Spinodal decomposition and nucleation and growth as a means to bulk nanostructured thermoelectrics: enhanced performance in $Pb_{1-x}Sn_xTe$–PbS, J. Am. Chem. Soc. 129 (2007) 9780.
[11] E. Quarez et al., Nanostructuring, compositional fluctuations, and atomic ordering in the thermoelectric materials $AgPb_mSbTe_{2+m}$: the myth of solid solutions, J. Am. Chem. Soc. 127 (2005) 9177.
[12] H. Wu et al., Ternary eutectic growth of nanostructured thermoelectric Ag–Pb–Te materials, Appl. Phys. Lett. 101 (2012) 23107.
[13] Silicon germanium thermoelectric materials and module development program (U), RCA Topical Report, Contract AT (29–2)-2510, 1969.
[14] J.P. Dismukes et al., Thermal and electrical properties of heavily doped Ge–Si alloys up to 1300 K, J. Appl. Phys. 35 (1964) 2899.
[15] G. Joshi et al., Enhanced thermoelectric figure-of-merit in nanostructured p-type silicon germanium bulk alloys, Nano Lett. 8 (2008) 12.
[16] P.D. Maycock, Thermal conductivity of silicon, germanium III–V compounds and III–V alloys, Solid State Electron. 10 (1967) 161–168.
[17] B. Abeles, D. Beers, G. Cody, J.P. Dismukes, Thermal conductivity of Ge–Si alloys at high temperatures, Phys. Rev. 125 (1962) 44–46.

[18] G.A. Slack, M.A. Hussain, The maximum possible conversion efficiency of silicon–germanium thermoelectric generators, J. Appl. Phys. 70 (1991) 2694–2718.

[19] B. Abeles, Lattice thermal conductivity of disordered semiconductor alloys at high temperatures, Phys. Rev. 131 (1963) 1906–1911.

[20] C.B. Vining, Thermoelectric properties of silicides 277, CRC Handbook of Thermoelectrics (Ed.) D.M. Rowe, CRC Press, London, 1995.

[21] S.K. Bux et al., Mechanochemical synthesis and thermoelectric properties of high quality magnesium silicide, J. Mater. Chem. 21 (2011) 12259.

[22] F.W. Dynys, A. Sayir, Self assemble silicide architectures by directional solidification, J. Eur. Ceram. Soc. 25 (2005) 1293.

[23] P. Ravishankar, Liquid encapsulated bridgman (LEB) method for directional solidification of silicon using calcium chloride, J. Cryst. Growth 94 (1989) 62.

[24] J. Schilz, V.N. Romanenko, Bulk growth of silicon-germanium solid solutions, J. Mater. Sci. Mater. Electron. 6 (1995) 265–279.

[25] L.M. Clark, R.E. Taylor, Radiation loss in the flash method for thermal diffusivity, J. Appl. Phys. 2 (1975) 714–719.

[26] PDF 01–072-6182 (ICDD, 2008).

[27] PDF 04–006-2527 (ICDD, 2005).

[28] A. Leineweber, E.J. Mittemeijer, Anisotropic microstrain broadening due to compositional inhomogeneities and its parameterisation, Z. Kristallogr. Suppl. 23 (2006) 117.

[29] K.A. Jackson, J.D. Hunt, Lamellar and Rod Eutectic Growth, Trans. Metall. Soc. AIME 236 (1966) 1128.

[30] B. Vinet et al., Correlations between surface and interface energies with respect to crystal nucleation, J. Colloid Interface Sci. 255 (2002) 363.

[31] S.V. Meschel, O.J. Kleppa, Standard enthalpies of formation of some 3d transition metal silicides by high temperature direct synthesis calorimetry, J. Alloys Comp. 267 (1998) 128.

[32] L.M. Levinson, Highly anisotropic columnar structures in silicon, Appl. Phys. Lett. 21 (1972) 15.

[33] D.M. Rowe, N. Savvides, The reversal of precipitation in heavily doped silicon-germanium alloys, J. Phys. D 12 (1979) 1613–1619.

[34] Z. Zamanipour, J.S. Krasinski, D. Vashaee, Comparison of boron precipitation in p-type bulk nanostructured and polycrystalline silicon germanium alloy, J. Appl. Phys. 113 (2013) 143715.

[35] T. Nonomura et al., Thermoelectric properties of group VI metal silicide semiconductors, Phys. Proc. 11 (2011) 110–113.

[36] S.V. Faleev, F. Leonard, Theory of enhancement of thermoelectric properties of materials with nanoinclusions, Phys. Rev. B 77 (2008) 214304.

[37] W. Parker, R. Jenkins, C.P. Butler, G.L. Abbott, Flash method of determining thermal diffusivity, heat capacity, and thermal conductivity, J. Appl. Phys. 32 (1961) 1679–1684.

[38] Y. Lee, G.S. Hwang, Microsegregation effects on the thermal conductivity of silicon-germanium alloys, J. Appl. Phys. 114 (2013) 174910.

[39] V.S. Neshpor, The thermal conductivity of the silicides of transition metals, J. Eng. Phys. Themophys. 15 (1968) 321–325.

[40] V. Arpaci, Conduction Heat Transfer, Addison-Wesley Pub. Co., 1966.